# Spherical Harmonics 3D Active Contours for Membrane Bilayer- Bound Surfaces

Khaled Khairy\*, Jacques Pecreaux\*, Jonathon Howard

Max-Planck Institute of Molecular Cell Biology and Genetics, Dresden, Germany

Abstract: Active contours is a powerful image segmentation technique based on simultaneously optimizing the overlap of a surface contour with the intensity image (external energy) on the one hand, and a constraining image-independent penalty based on the first and second derivatives of the contour (internal energy) on the other. Although the above form is applicable to a wide class of images, including prior information about the topology and smoothness as well as insights from physical theories regarding specific material properties of the object under study are expected to result in faster and more accurate segmentations.

In this work we extend the formulation of the active contour internal energy for the common case of 3D-imaging lipid-bilayer membrane-bound objects of topological genus zero. Examples include organelles, cells and artificial vesicles. In the non-supervised method presented here, the internal energy takes into account membrane bending elasticity as well as constraints imposed by the fact that the two bilayer leaflets are allowed to slide relative to each other. An additional topology constraint is implicitly accounted for by using a spherical harmonics parametric contour representation. The balance between internal and external energies (i.e. the regularization parameter) is determined using the L-curve method.

To ensure convergence and numerical stability a good starting guess for the contour is essential. We show in detail a method, that also makes use of the L-curve, for calculating this guess, and apply the complete procedure to a representative synthetic data set using realistic physical quantities based on membrane biophysical theories and known experimental results.

## 1 Introduction

Active contours [1] have been used extensively as a means for automatic and accurate image segmentation. The main idea is to allow a contour that is superimposed on the image to change shape until it minimizes a cost functional (*E*) that takes the form

<sup>\*</sup> These authors contributed equally to this work.

$$E = E_{\text{internal}} + \lambda E_{\text{external}} \tag{1}$$

with  $E_{\text{internal}}$  a shape prior that enforces smoothness constraints and typically depends on the first and higher derivatives of the contour,  $E_{\mathrm{external}}$  a quantity sensitive to the amount of overlap of the contour with the intensity values of the image, and  $\lambda$  a parameter that balances the relative importance of the two terms. Equation 1 is generally applicable in 2 and 3 space dimensions. Implementations of the method differ in the choice for  $\lambda$ , the exact forms for  $E_{\mathrm{internal}}$  and  $E_{\mathrm{external}}$ , and the mathematical description of the contour. Subjective choices of  $\lambda$  and physically unrealistic forms for  $E_{\text{internal}}$  result in convergence to suboptimal shapes. This problem has partially been alleviated by the introduction of statistical shape models (see for example [2]), which constrain the contour search to a subset of the shapes allowed by the shape description. However, statistical shape models require a training set and may impose constraints that are too stringent for detecting significant variations in shape. Most importantly, they generally do not provide a natural connection to the underlying biophysics that gave rise to a particular shape. Therefore we will address the issue of segmenting 3D intensity images in the context of Equation 1, when the object under study has —at least partially —known mechanical properties.

## 1.1 Incorporation of Prior Information into the Active Contour Procedure

In this paper, we focus on objects that are bounded by lipid membrane bilayers. Examples include organelles, cells and artificial bilayer vesicles (liposomes). For these objects biophysical theories [3] and experimental mechanical measurements [4-6] provide prior information that can be incorporated into our edge-finding procedure. The theoretical predictions alone are already able to reproduce shapes that closely resemble experimental observations both qualitatively [7] and quantitatively [8] in cases where the membrane bilayer is expected to primarily determine the morphology (Fig.1a).

 $E_{\rm internal}$  of Equation 1 is an appropriate vehicle for incorporating such prior information [9], which primarily depends on the membrane bending elasticity and the resistance of the area difference between the bilayer leaflets to deviate from some preferred value (Fig.1b). Fig.1a shows some of the "default" shapes that the active contour will tend to when such an  $E_{\rm internal}$  is minimized on its own.

Moreover, the topology of such biological objects is often restricted to that of the sphere. This piece of prior information we implicitly include by using a spherical harmonics parameterization (SHP) of the surface [10]. The spherical harmonics are the 3D equivalent of the Fourier series defined on the surface of a sphere (see below).

## 1.2 Other Issues: Regularization and the Starting Shape

To avoid artificially favoring  $E_{\rm internal}$  over  $E_{\rm external}$  or vice versa, we use an objective way for determining the regularization parameter  $\lambda$  in Equation 1, namely the L-curve method [11], which determines  $\lambda$  as the point of maximum curvature on the curve obtained when plotting the logarithm of  $E_{\rm internal}$  vs. the logarithm of  $E_{\rm external}$  when performing the optimization for a series of values of the regularization parameter.

However, before optimizing Equation 1, we need a good starting set of shape coefficients to improve convergence and numerical stability. To obtain such a set we map an initial surface triangulation (obtained for instance by using a marching cubes algorithm) to the unit sphere [12, 13]. In this article we introduce a method of spherical mapping that also benefits from the objectivity of the L-curve procedure.

Our complete method is illustrated on a noisy synthetic 3D intensity data set that simulates 3D fluorescence microscopy images of a human red blood cell discocyte. To our knowledge, this is the first demonstration of 3D active contours based on membrane biophysics.

## 2 Theory

## 2.1 Membrane-biophysics-derived (internal) Energies

Here we give the expressions used to calculate the internal (image-independent) energy of the contour, when we know that the observed object is bounded by a lipid-bilayer membrane. Theoretically the shape of a membrane bilayer contour is assumed to minimize an energy functional (E) that –among other possible contributions—includes the bending energy of the membrane  $(E_b)$  [14], and the area difference elasticity energy  $(E_{ADE})$ , which is the resistance of the area difference between the outer and inner leaflets  $(\Delta A)$  to deviations from some preferred value  $(\Delta A_o)$ [15-18].

$$E_{\text{internal}} = E_b + E_{ADE} \tag{2}$$

The first term is given by,

$$E_b = \frac{\kappa_b}{2} \oint_{S} (2H - C_o)^2 dA \tag{3}$$

where  $\kappa_{\rm b}$  (~25x10<sup>-20</sup>J [5]) is the bending modulus, H is the local curvature, and  $C_o$  is the preferred curvature.  $C_o$  is a local term that depends on the local lipid composition and lipid molecule geometry (Fig.1b). The second term in Equation 1 is given by

$$E_{ADE} = \frac{\overline{\kappa}\pi}{2AD^2} \left(\Delta A - \Delta A_o\right)^2 \tag{4}$$

where A is the total surface area of the contour, D is the separation between the two bilayer leaflets and  $\overline{K}$  is a global elastic modulus. The relative importance of  $E_{\rm b}$  vs.  $E_{\rm ADE}$  is controlled by the ratio  $\alpha = \overline{K} / \kappa_b \simeq 2/\pi$  [7]. Equation 4 constitutes a global term, justified by the fact that the two bilayer leaflets are allowed to slide relative to each other, so the effect of –for example- adding lipid molecules to one of the leaflets, would be an instantaneous redistribution of this perturbation over the whole shape (Fig.1b). In the preceding Equations, all integrations are performed over the closed surface  $\vec{S}$ .  $C_o$  and  $\Delta A_o$  cannot be independently determined and are mathematically not separable [19]. They enter the calculation through a unitless effective preferred area difference parameter  $\Delta a_o = \Delta A_o / A + \kappa_b D C_o / \pi \overline{\kappa}$ . Typically  $\Delta a_o$  varies between 0.2 and -0.2, and considerably influences the default shape (see [7] and Figure 1a).

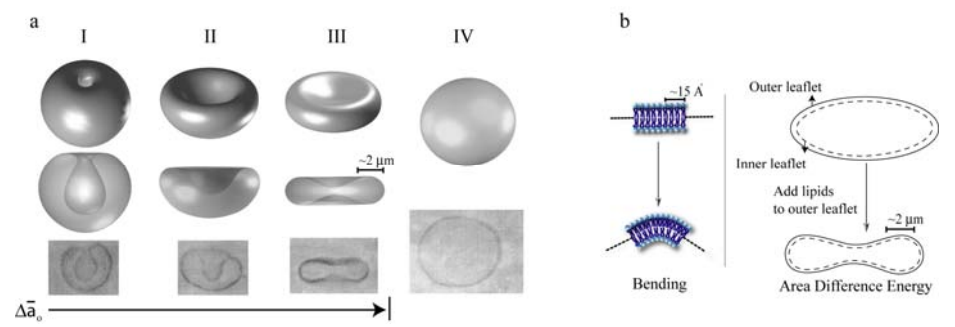


**Fig.1.** Shape energy and typical predicted shapes. (a) Theoretically predicted minimum energy shapes considering bending and area difference elasticities under constraints of total surface area and volume. Going from contour I to III,  $\Delta \overline{a_o}$  the parameter responsible for the preferred curvature and preferred area difference between the two bilayer leaflets is increased, while keeping the area and volume constraint the same. Contour IV shows that the theory can also predict nearly spherical shapes given the appropriate ratio of area to volume. Images shown in the bottom row are reproduced from [3] (b) Schematic of lipid bilayer showing the two main energy contributions entering the calculation of shape energy; bending and area difference elasticities.

## 2.2 External energy

Our external energy term follows the Chan et Vese formulation [20] based on the Mumford-Shah approach [21]

$$E_{\text{external}} = \int_{\text{innerVolume}} \lambda_{\text{in}} (I - c_{\text{in}})^2 dV + \int_{\text{outerVolume}} \lambda_{\text{out}} (I - c_{\text{out}})^2 dV$$
 (5)

where I is the image intensity, V the volume,  $c_{\rm in}$  and  $c_{\rm out}$  are the average intensities inside and outside the contour respectively, and  $\lambda_{\rm in}$  and  $\lambda_{\rm out}$  are hyperparameters.

#### 2.3 Spherical harmonics surface parameterization

A function r of the spherical coordinates  $(\theta, \phi)$  may be represented as a series expansion,

$$r(\theta, \phi) = \sum_{L=0}^{\infty} \sum_{K=-L}^{L} C_{LK} y_{LK}(\theta, \phi)$$

$$\tag{6}$$

where  $0<\theta<\pi$  and  $0<\phi<2\pi$ . The  $C_{LK}$  s are the expansion coefficients, indexed by the integers L and K with  $-L \le K \le L$  and  $0 \le L \le \infty$ .  $y_{LK}(\theta,\phi)$  are the spherical harmonics basis functions defined by

$$y_{LK}(\theta, \phi) = N_{LK} P_{LK}(\cos \theta) \cos(K\phi)$$
 when  $K \ge 0$ , (7)

and

$$y_{LK}(\theta, \phi) = N_{LK} P_{LK}(\cos \theta) \sin(|K|\phi)$$
 when  $K < 0$ , (8)

where  $P_{L,K}(\cos\theta)$  are the associated Legendre polynomials and  $N_{LK}$  are normalization constants. The  $y_{LK}(\theta,\phi)$ s form a complete othogonal basis set of well known properties [22]. The above representation is limited to surfaces (described as stellar surfaces) that contain an interior point that can be connected to every point on the surface by a straight line without intersecting the surface. We represent a general (stellar or non-stellar) surface  $\vec{S}$  that is topologically equivalent to the sphere parametrically by expanding its individual Cartesian coordinates using spherical harmonics series,

$$\vec{S}(\theta,\phi) = \begin{bmatrix} x \\ y \\ z \end{bmatrix} = \begin{bmatrix} X(\theta,\phi) \\ Y(\theta,\phi) \\ Z(\theta,\phi) \end{bmatrix}$$
(9)

where  $X(\theta,\phi)$ ,  $Y(\theta,\phi)$  and  $Z(\theta,\phi)$  are individually expanded using Equation 6, giving three sets of expansion coefficients ( $C_{LK}^X$ ,  $C_{LK}^Y$ ,  $C_{LK}^Z$ ) which completely define the shape. The numerical implementation of SH calculations necessitates choosing a series truncation ( $L_{max}$ ). Also, given a set of data points, the  $C_{LK}$ s are calculated according to,

$$C_{LK}^{X} = \int_{0}^{2\pi} \int_{0}^{\pi} X(\theta, \phi) y_{LK}(\theta, \phi) \sin \theta d\theta d\phi$$
 (10)

with similar equations for  $Y(\theta, \phi)$  and  $Z(\theta, \phi)$ . It should be noted that the SHP is particularly economical and is not confined to any particular symmetry.

## 2.4 Balancing internal and external energies: the L-curve method

The regularization parameter  $\lambda$  in Equation 1, determines the balance between our prior information about the observed object (usually a smoothing function), expressed through the internal energy, on the one hand, and fitting of the contour to the image data (also called the residual function), our external energy, on the other. An objective procedure for choosing  $\lambda$  is the L-curve method [11]. It is constructed by plotting the logarithm of the residual function vs. the logarithm of the smoothing function for a sufficiently large range of  $\lambda$  values. The optimal regularization parameter value corresponds to the point of maximum curvature on this usually L-shaped curve, which we determine graphically (Fig.3b). If an L-curve calculation does not give the proper vertical part of the "L", then the series is artificially (implicitly) over-truncated and the series truncation must be relaxed to include higher order coefficients. On the other hand, if the L-curve is missing the horizontal part then the theoretical prediction (encoded in  $E_{\text{internal}}$ ) coincides with the actual contour, and one could conclude that the shape is accounted for completely by the theory.

Note that we also use the L-curve method in this work in the context of finding the optimal spherical mapping for the determination of a starting guess (Fig.2f) (see Section 3.2).

## 3 Computational Methods

## 3.1 Method Overview

We begin by generating a starting guess of our surface contour, where the 3D fluorescence image is thresholded using Laplacian-of-Gaussian zero-crossing edge detection [23]. From the resulting point-cloud a surface triangulation is generated that must not contain small handles or holes. This is followed by uniformly mapping the surface to a unit sphere so that Equation 10 can be applied, to calculate three series expansions corresponding to the individual x, y and z coordinates. The coefficients of these expansions form the starting parametric approximation of the surface, which is then refined by iteratively minimizing the energy expression of Equation 1. We assume that changes to the coefficients introduced throughout the fitting are small enough so a modification of the initial spherical mapping is not necessary. The minimization is repeated for a sufficient range of  $\lambda$  values and an L-curve is constructed. Our final surface is the one fitted with the  $\lambda$  value that corresponds to the corner of the L-curve, which we determine graphically. The calculation of the internal energy necessitates evaluation of A, V, and B of the surface, for which we use the expressions in [24]. Our formula for calculating the external energy is given in the

Appendix. For the minimization of Equation 1 we used the downhill simplex (Simplex) algorithm [25]. Below we provide details regarding the spherical mapping.

## 3.2 The Spherical Mapping Step

Starting with the surface triangulation, each surface point (x, y, z) must be mapped onto a point  $(\theta, \phi)$  on the surface of the unit sphere, while maintaining connectivity and nearest neighbors, preserving relative triangle areas and minimizing triangle shear deformation. We demonstrate our procedure for accomplishing this on the spherical mapping of the triangulated surface of a letter E (Fig.2a).

The first step in the topological mapping is a rough mapping of surface points to the unit sphere conserving connectivity. We follow the method of [10] after modifying it for surface triangulations. In short, two poles (vertices) are chosen on the surface mesh. One is identified as the "North pole" ( $\theta_N$ ) and the second as the "South pole" ( $\theta_S$ ). For assigning a (latitude)  $\theta$  value, a Laplace equation  $\nabla^2\theta=0$ , with Dirichlet conditions  $\theta_N=0$  and  $\theta_S=\pi$  is solved, (a stationary heat diffusion equation) (Fig.2b). To calculate (longitude)  $\phi$ , a date line is introduced along which  $\phi$  is incremented or decremented by  $2\pi$ , and the cyclic Laplace equation is then solved (Fig.2c). Now each vertex has associated with it a unique  $(\theta,\phi)$  coordinate and can be placed on the unit sphere (Fig.2d).

For a proper final shape representation the vertices must be uniformly distributed on the unit sphere. As a starting point, we use a modified version of equation 6 in [12]. The problem is to minimize

$$\sum_{i}^{m} \left[ \left( \frac{a_{p,i}}{4\pi} - \sum_{i}^{a_{o,i}} a_{o,i} \right)^{2} + \gamma \beta_{i}^{2} \right]$$
 (11)

where  $a_{p,i}$  is the geodesic area of triangle i=1,2,...,m, on the parametric sphere,  $a_{o,i}$  is the area of triangle i on the original object,  $\beta_i$  is the measure of shear deformation of triangle i when mapping from object to parameter space, calculated from the local principal stretches  $\lambda_{i,l}$  and  $\lambda_{i,2}$  [26],  $\beta_i = (\lambda_{i,1} - \lambda_{i,2})^2 / 2\lambda_{i,1}\lambda_{i,2}$ , and  $\gamma$  is a scaling factor that controls the linear combination and is in essence a regularization parameter. The first term in Edquation 11 drives the optimization to equate the relative triangle areas in both object and parameter spaces. The second term measures the extent of deformation of individual triangles relative to their undeformed state, which is the configuration in object space. The optimization of Equation 11 is performed for a series of  $\gamma$  values and an L-curve is constructed (Fig. 2f). The resulting mapping, when  $\gamma$  is chosen properly, is uniform (Fig.2e), and is used to calculate the coefficients according to Equation 10 (Fig.2g middle). Non-optimal choices of  $\gamma$  result in deformed surfaces that are unrealistic and unsuitable as starting shapes (see Figure 2g left and right).

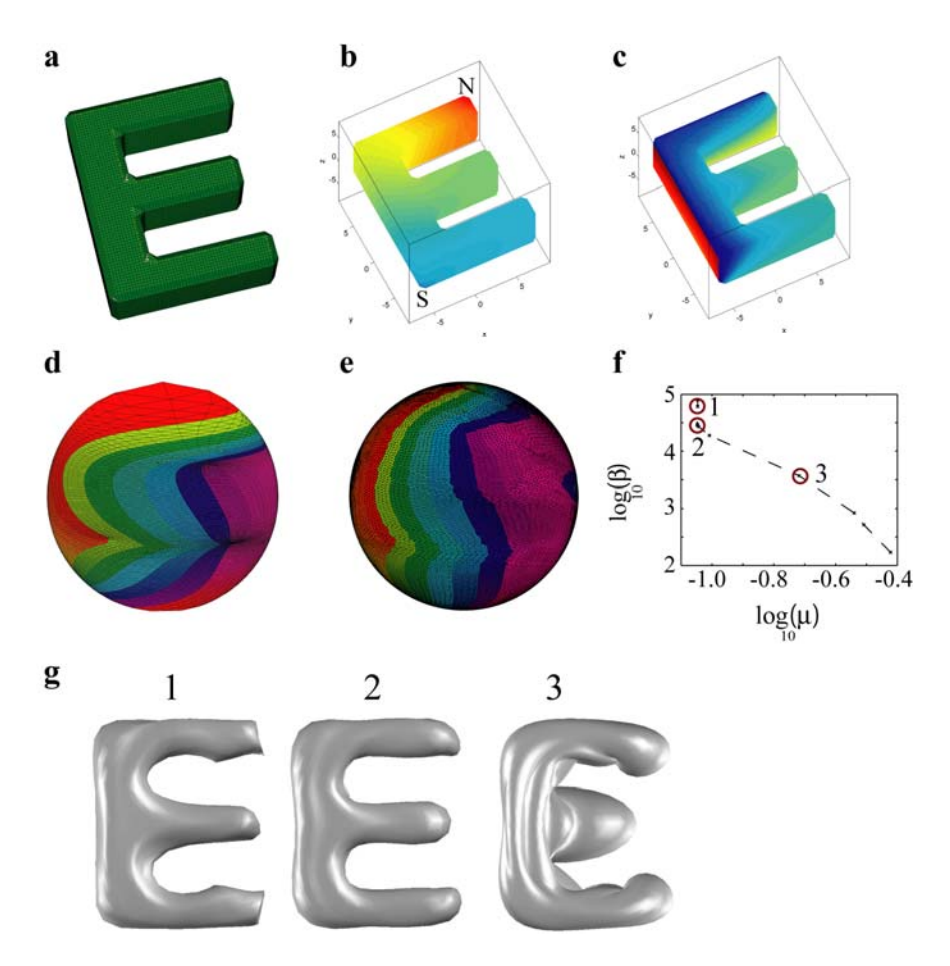


**Fig.2. Spherical Mapping.** Parameterization of the letter E by minimization of the balance between area dilation and shear deformation. (a) Surface triangulation of the capital letter E, (b) assignment of values for longitude ( $\theta$ ) and (c) latitude ( $\phi$ ) to the vertices by solving the stationary heat equation, which provides the initial mapping of the vertices onto the unit sphere, (d)  $\theta$ ,  $\phi$  configuration in parameter space before performing the mapping optimization (e)  $\theta$ ,  $\phi$  configuration in parameter space after performing the mapping optimization for the  $\gamma$ -value corresponding to the corner of the L-curve in (f), (f) L-curve for finding the optimal  $\gamma$ -value (Equation 11) that balances area preservation  $\mu$  (first term in Equation 11) and polygon deformation  $\beta$  (the second term), (g) shape models constructed by expanding the Cartesian coordinates in SH at an expansion truncation of  $L_{\rm max} = 10$ , after optimization of Equation 11 for three different values of  $\gamma$  (corresponding to marked positions on the L-curve in (f)), number 2 is the one with the best  $\gamma$ .

## 4 Results and Discussion

We demonstrate our proposed scheme for biophysics-guided 3D global parametric active contours on a synthetic 3D fluorescence microscopy data set.

## 4.1 Recovery of a known Shape from noisy 3D Pseudo-image Data

We constructed a noisy 3D synthetic intensity data set that mimics imaging a membrane bilayer-labeled discocytic surface under conditions typical for confocal fluorescence microscopy (Fig.3a). The discocyte surface was originally generated with  $L_{\rm max}=3$ . This surface is of minimum (internal) energy at  $\Delta \overline{a_o}=0.00143$ , for typical values of bending and area difference moduli (see Section 2.1) and under the constraints  $A=140~\mu{\rm m}^2$  and  $V=100~\mu{\rm m}^3$ .

To test the consistency of our method, we applied it to the recovery of the discocyte shape from the noisy data set. We allowed spherical harmonic coefficients up to order  $L_{\text{max}} = 22$  as free parameters to be fitted, and repeated the optimization for decreasing values of  $\lambda$  ranging from  $10^4$  to  $10^{-1}$ . At high  $\lambda$  the optimization finds coefficients that minimize the overlap of the contour with the noisy image, resulting in an unrealistic bumpy surface (Fig.3 b contour I). As  $\lambda$  decreases the surface gradually gets smoother (Fig.3 b contour II) until the corner of the L-curve is reached (Fig.3 b contour III).

When we performed these calculations with the correct (to us known beforehand)  $\Delta \overline{a_o}$  value of 0.00143, all further points on the curve coincided with the (now) corner point shown and no L-shaped curve was obtained. This is expected because with the correct biophysical parameters the shape will converge to the discocyte, driven by the internal energy alone, independent of the image, which in this case happens to be the image of the same shape, so no further degradation of the image term occurs. However, in the general case  $\Delta \overline{a_o}$  is not accurately known, so in order to test whether our method is robust against deviations of  $\Delta \overline{a_o}$  from its true value, we repeated the calculation with  $\Delta \overline{a_o} = 0.0005$ , obtained the L-curve shown, and registered a clear corner that corresponds to the (smooth) discocyte. Further decrease in  $\lambda$ , led to the appearance of an elongated shape that minimized the internal energy under the given (guessed)  $\Delta \overline{a_o}$ .

## 5. Conclusion

In this work we extended the applicability of the method of biophysically-based active contours to image segmentation of membrane bilayer-bound objects into three space dimensions using the spherical harmonics parametric shape description. The

prior information about shape contour topology is incorporated implicitly in our choice of shape description. Our prior information about the mechanics of the membrane and its smoothness is explicitly formulated in an image-independent internal energy term that incorporates principal results from membrane biophysics theories and experimental membrane mechanics measurements. We also introduced a method for the step of initial spherical mapping. The regularization parameter needed for both the active contours and the spherical mapping optimizations was determined using the L-curve method. We demonstrated the applicability of our method using a realistic synthetic 3D image data set.

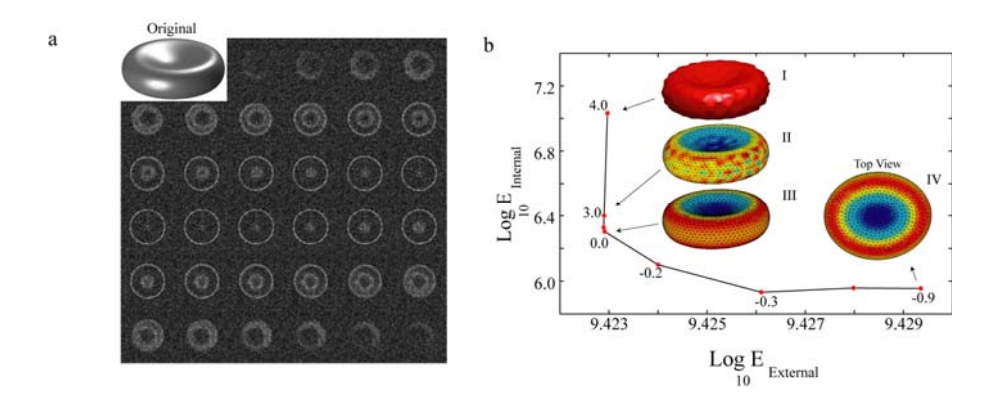


Fig.3. Recovery of a discocyte from noisy synthetic data. (a) Synthetic noisy image stack based on a slightly tilted discocyte surface ( $L_{\text{max}}$ = 3) (shown in the inset), convolved with a theoretically calculated point spread function. (b) L-curve for a range of  $\lambda$  values (from  $1\times10^4$  to  $1\times10^{-1.0}$ ). The starting shape was obtained by spherical mapping with  $L_{\text{max}}$ = 22, numbers next to the data points represent  $\log_{10}(\lambda)$ . To obtain this L-curve,  $\Delta \overline{a_o}$  of 0.0005 was used instead of the true value 0.00143. At small  $\lambda$  values the discocytic shape changes to an elliptocyte (the default shape at this  $\Delta \overline{a_o}$  value). At high  $\lambda$  the external energy dominates and because high expansion orders were allowed, the surface tries to fit the noise, and becomes irregular. The optimal surface is found at the corner of the L-curve.

**Acknowledgements** This work was funded by the Max-Planck Society. J. Pecreaux's work was also funded by the Human Frontier Science Program Organization.

## References

- 1. Kass, M., A. Witkin, and D. Terzopoulos, *Snakes: active contour models*. International Journal of Computer Vision, 1988. 1: p. 321-331.
- 2. Cootes, T., et al., *Active shape models their training and application*. Computer vision and image understanding, 1995. **61**: p. 38-59.
- 3. Lipowsky, R., *The conformation of membranes*. Nature, 1991. **349**: p. 475-481.

- 4. Waugh, R. and R. Bauserman, *Physical measurements of bilayer-skeletal separation forces*. Ann Biomed Eng, 1995. **23**(3): p. 308-21.
- 5. Strey, H., M. Peterson, and E. Sackmann, *Measurement of erythrocyte membrane elasticity by flicker eigenmode decomposition*. Biophys J, 1995. **69**(2): p. 478-88.
- 6. Scheffer, L., et al., *Atomic force pulling: probing the local elasticity of the cell membrane.* European Biophysics Journal, 2001. **30**(2): p. 83-90.
- 7. Lim, H.W.G., M. Wortis, and R. Mukhopadhyay, Stomatocyte-discocyte-echinocyte sequence of the human red blood cell: evidence for the bilayer-couple hypothesis from membrane mechanics. Proc Natl Acad Sci USA, 2002. 99(26): p. 16766-9.
- 8. Doebereiner, H.G., et al., *Mapping vesicle shapes into the phase diagram: A comparison of experiment and theory.* Phys. Rev. E, 1997. **55**(5): p. 4458-74.
- 9. Pecreaux, J., C. Zimmer, and J. Olivo-Marin. *Biophysical Active Contours for Cell Tracking I: Tension and Bending*. in *ICIP 2006*. 2006. Atlanta, USA
- 10. Brechbühler, C., G. Gerig, and O. Kuebler, *Parametrization of closed surfaces for 3-D shape description*. Comput Vision Image Und, 1995. **61**(2): p. 154-170.
- 11. Hansen, P.C., Rank-deficient and discrete ill-posed problems: numerical aspects of linear inversion. 1997, Philadelphia: SIAM.
- 12. Quicken, M., et al. Parameterization of Closed Surfaces for Parametric Surface Description. in IEEE Computer Society Conference on Computer Vision and Pattern Recognition CVPR 2000. 2000: IEEE Computer Society.
- 13. Shen, L. and F. Makedon, *Spherical mapping for processing of 3D closed surfaces*. Image and vision computing, 2006. **24**: p. 743-761.
- 14. Deuling, H.J. and W. Helfrich, *Red blood cell shapes as explained on the basis of curvature elasticity*. Biophys J, 1976. **16**(8): p. 861-8.
- 15. Sheetz, M.P. and S.J. Singer, *Biological membranes as bilayer couples*. Proc Natl Acad Sci USA, 1974. **71**: p. 4457-4461.
- 16. Seifert, U., K. Berndl, and R. Lipowsky, *Shape transformations of vesicles: Phase diagram for spontaneous- curvature and bilayer-coupling models.* Phys Rev A, 1991. **44**(2): p. 1182-1202.
- 17. Heinrich, V., S. Svetina, and B. Zeks, *Non-Axisymmetric Vesicle Shapes in a Generalized Bilayer-Couple Model and the Transition between Oblate and Prolate Axisymmetric Shapes.* Phys Rev E, 1993. **48**(4): p. 3112-3123.
- 18. Miao, L., et al., *Budding transitions of fluid-bilayer vesicles: The effect of area-difference elasticity.* Phys Rev E, 1994. **49**(6): p. 5389-5407.
- 19. Mukhopadhyay, R., H.W.G. Lim, and M. Wortis, *Echinocyte shapes: bending, stretching, and shear determine spicule shape and spacing.* Biophys J, 2002. **82**(4): p. 1756-72.
- 20. Chan, T.F. and L.A. Vese, *Active Contours without edges*. IEEE Transactions on image processing, 2001. **10**(2): p. 266-277.
- 21. Mumford, D. and J. Shah, *Optimal Approximations by Piecewise Smooth Functions and Associated Variational-Problems*. Communications on Pure and Applied Mathematics, 1989. **42**(5): p. 577-685.

- 22. Hobson, E.W., *The theory of spherical and ellipsoidal harmonics*. 1955, New York: Chelsea.
- Marr, D. and E.C. Hildreth, *Theory of edge detection*. Proc R Soc Lond Ser B, 1980. 207: p. 187-217.
- Julicher, F., Die Morphologie von Vesikeln. 1993, University of Cologne. p. 131.
- 25. Nelder, J.A. and R. Mead, *A simplex method for function minimization*. Comput J, 1965. 7: p. 308.
- 26. Evans, E.A. and R. Skalak, *Mechanics and Thermodynamics of Biomembranes*. 1980, Boca Raton, FL: CRC.

## Appendix: Calculation of $E_{\text{external}}$

In analogy with electrostatics, one can write an "electric" field  $\vec{E}_{\rm in}$  and  $\vec{E}_{\rm out}$  corresponding to a distribution of charge  $(I-c_{\rm in})^2$  and  $(I-c_{\rm out})^2$ . Using the Gauss theorem,

$$E_{\rm external} = \lambda_{\rm in} \int_{\rm surface} \vec{E}_{\rm in}.d\vec{N} + \int_{\rm image} (I - c_{\rm out})^2 dV - \lambda_{\rm out} \int_{\rm surface} \vec{E}_{\rm out}.d\vec{N} \tag{A-1}$$

where 
$$d\vec{N} = \frac{\partial S}{\partial \theta} \times \frac{\partial S}{\partial \varphi}$$
 is the local surface normal.

This approach would necessitate a careful and precise solution of the Poisson equations for the potential from which  $\vec{E}_{\rm in}$  and  $\vec{E}_{\rm out}$  are derived. Such a treatment is beyond the scope of this paper, so for the sake of practicality we compute the value of the image at the contour positions by an integration of the functional derivative of the external energy,

$$\frac{\delta E_{\text{external}}}{\delta S} = \lambda_{\text{in}} \int_{\text{surface}} \text{div } \vec{E}_{\text{in}} d\vec{N} - \lambda_{\text{out}} \int_{\text{surface}} \text{div } \vec{E}_{\text{out}} d\vec{N}$$
 (A-2)

This only requires the computation of the surface normals using the image value on the surface only, which makes the computation more efficient.